Journal of Materials Chemistry A

ROYAL SOCIETY OF CHEMISTRY

PAPER

View Article Online
View Journal | View Issue

Cite this: J. Mater. Chem. A, 2024, 12, 30862

A matter of design and coupling: high indoor charging efficiencies with organic solar modules directly coupled to a sodium ion battery†

Li-Chung Kin, *[ab] Andreas Distler, [c] Oleksandr Astakhov, [d] Bakary Kone,[d] Hans Kungl,[a] André Karl, [a] Tsvetelina Merdzhanova, *[d] Rüdiger-A. Eichel, [ae] Christoph J. Brabec [cf] and Uwe Rau [bdg]

Received 8th July 2024
Accepted 24th September 2024

DOI: 10.1039/d4ta04729j

rsc.li/materials-a

To tackle the challenge of powering distributed autonomous indoor sensors and electronics, such as in the implementation of the internet of things (IOT), a high-efficiency solar module with integrated storage is a potential solution that offers a stable, reliable power source. For this, organic photovoltaics (OPV) are a promising candidate, delivering high efficiencies under indoor lighting, flexibility, scalability and low-cost designs *via* roll-to-roll manufacturing. Pairing an OPV device with batteries made from widely available sodium seems to be a viable strategy for achieving a low-cost, low-power, self-charging power source. PV devices can be coupled directly to batteries without power conditioning. Self-sustained operation and stable power output of this power harvester are achievable with proper voltage matching and scaling of both the PV and battery within the target range of operating conditions. We achieved a record indoor direct charging overall efficiency of an OPV and sodium ion battery of 13.1–14.4% over a wide range of LED illumination intensities of 150–15 000 lx.

Introduction

Remote indoor energy harvesting[1–10] is a promising way to power distributed light and temperature sensors in an office or home without the need for additional wiring or single use battery cells. As demonstrated in previous studies, perovskite solar cells (PSC) are already shown to be very promising and feasible for indoor applications.[1] In the present study, a similar approach is employed using an OPV in combination with a sodium ion battery.

Recent advances in organic photovoltaics have shown individual cell power conversion efficiencies approaching 20% under 1 sun,[11–14] with OPV modules having progressed to reaching efficiencies beyond 14%.[15–20] Even though PSCs exceed OPV performance in terms of indoor efficiency,[1,2,21] the overall stability is still on average better for OPVs. Furthermore, recent studies have shown the potential of organic photovoltaics (OPVs) for use in indoor energy harvesters as a sustainable, environmentally friendly, and fully recyclable technology with a tuneable band gap.[5,22–28] In addition, they have the potential for large scale roll-to-roll manufacturing[5–7,23,25,29] and have been shown to be capable of operating off-grid micro devices under ambient light.[30,31] OPVs are already broadly manufactured,[32] and their costs, production and operational lifetime are very comparable to those of amorphous silicon, which is still state of the art for indoor PV applications.[33–35] Therefore, OPVs are a viable alternative technology for indoor energy harvesting.

The absorption spectra of many state-of-the-art absorber layers in OPV materials exhibit good overlap with the spectral irradiance of modern indoor lights such as LEDs and compact fluorescent tubes.[22,29,36,37] In particular, the PM6:Y6 absorbance spectrum overlaps the AM1.5 spectrum very well[38] and fully covers the LED spectrum of commercially available LEDs (Fig. S1†). Theoretical estimates for the efficiency limit of a single junction solar cell made under illumination with the narrower spectrum of LEDs result in a higher optimal band gap of approximately 1.8–1.9 eV and theoretical efficiencies exceeding 50%,[39–44] both values being higher than those for the solar spectrum. Single OPV cells exceeding 30% PCE under concentrated indoor LED illumination have been reported[45,46]

[a]Institut für Energie- und Klimaforschung (IEK-9), Forschungszentrum Jülich GmbH, 52428 Jülich, Germany. E-mail: l.kin@fz-juelich.de
[b]Faculty of Electrical Engineering and Information Technology, RWTH Aachen University, Mies-van-der-Rohe-Straße 15, 52074 Aachen, Germany
[c]Institute Materials for Electronics and Energy Technology (i-MEET), Department of Material Science, Faculty of Engineering, Friedrich-Alexander-Universität Erlangen-Nürnberg, Martensstraße 7, 91058 Erlangen, Germany
[d]Institut für Energie- und Klimaforschung (IEK-5), Forschungszentrum Jülich GmbH, 52428 Jülich, Germany. E-mail: t.merdzhanova@fz-juelich.de
[e]RWTH Aachen University, Mies-van-der-Rohe-Straße 15, 52074 Aachen, Germany
[f]Helmholtz Institute Erlangen-Nürnberg for Renewable Energy (HI-ERN), Forschungszentrum Jülich GmbH, Immerwahrstraße 2, 91058 Erlangen, Germany
[g]Jülich Aachen Research Alliance (JARA-Energy), Faculty of Electrical Engineering and Information Technology, RWTH Aachen University, Schinkelstr. 2, 52062 Aachen, Germany

† Electronic supplementary information (ESI) available. See DOI: https://doi.org/10.1039/d4ta04729j

with many examples exceeding 10% under various intensities.[26,47] As such, indoor and outdoor efficiencies follow different optimization criteria, as will be further discussed in this work.

Design and optimization of indoor PV devices is challenging due to intermittent and low output power, varieties of illumination spectra and a high dynamic range of light intensities. An indoor device can experience illumination ranging from approximately one sun when irradiated by direct sunlight down to a few lux received from a distant light in a dark room. Furthermore, there is no established measurement standard procedure for indoor devices. Thus, it is imperative to measure the cell across a wide range of illumination intensities with a focus on lower illumination intensities of 150 lx to 500 lx, typical of office conditions.[48]

The variable lighting scenario makes it difficult to utilize indoor lighting and necessitates a battery to stabilize the output of the indoor PV harvester. Attempts to utilize the intermittent nature of PV energy directly to charge a battery, without the use of power electronics, have been met with various degrees of success both in integrated devices and in discrete devices connected by wires (Table S1†).[33,49–55] However, most such attempts so far involve 1 sun irradiance for outdoor use and indoor examples are limited. Overall efficiency of the reported OPV-battery systems under indoor conditions remains in the low single digit range, not exceeding 2% overall efficiency so far.[56] The low efficiency is despite both the PV and battery performing well under separate standardized tests done prior to being used together and the absence of any obvious problems that would lead to the loss of half of the PV efficiency.

The rift in the performance between the individual components and that of the PV-battery device usually stems from two types of mismatch. The first is the voltage mismatch between the maximum power point of a PV device and the operating voltage of a battery, resulting in under-performing PV energy delivery or insufficient voltage to fully charge the battery. Second is the power mismatch between the solar module and the battery capabilities, resulting in high overpotentials (storage voltage losses) from either poor rate capability[57] or from excessively high C-rates for the battery.[55,58] Both have to be addressed in the design stage of the experiment for high overall efficiency.

Given the target of powering numerous indoor always-on devices, generally known as the 'internet of things' (IoT), the battery technology for an integrated device needs to be produced from cheap, sustainable sources, such as sodium ion batteries. For efficient operation of an integrated device, the sodium ion chemistry is high rate capable and has low overpotentials to minimize mismatch effects. This will result in a larger operating window of illumination, high current pulse discharge, increased safety against overcharge under varying light intensity and the capability to use a smaller battery as higher current densities can be achieved.

In this paper, using a discrete sodium ion battery directly charged by an organic solar module, we show overall efficiencies exceeding 10% under low indoor illumination for the first time. The design was optimized to operate efficiently and safely across a wide range of LED illumination intensities from 150 to 15 000 lx relevant for indoor applications. Finally, we focus on the aspects of PV-battery matching for indoor applications and formalize a general design framework to guide future PV-battery integration.

Results and discussion

Pre-test characterisation

OPV module characterization. The OPV module is based on the active material system PM6:Y6:PCBM,[38] which is currently among the best-performing systems for large-area OPV modules.[59] Its layout, which is described in detail in the Experimental section, was specifically adapted to our application of charging a battery under low-light conditions.

The 5-cell module was characterized under increasing LED illumination intensities from 150 lx to 15 000 lx (Fig. 1a and b) and under 1 sun/AM1.5 (Table S2 and Fig. S2†). Specific values for the lowest and highest irradiance were extracted and are shown in Table 1 alongside the 1 sun performance on the rightmost column. It was deduced that the maximum power point voltage across the entire range of applied illumination intensities varies between 2.1 and 2.5 V and that the maximum current the battery will experience does not exceed 5 mA at the most intense LED illumination.

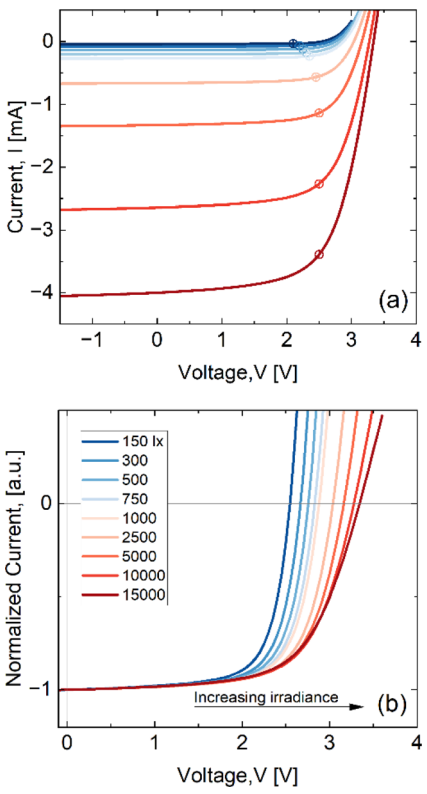

Fig. 1 (a) Current–voltage curves for the 5-cell PM6:Y6:PCBM module under different warm white (3000 K) LED illumination from 150 to 15 000 lx. Maximum power points are marked for each curve by the corresponding circles. (b) Current voltage curves normalized to the short-circuit current for each curve.

Table 1 PV parameters of the OPV solar module with 5-cells based on PM6:Y6:PCBM (from left to right) characterised under a 3000 K warm white LED (150 and 15 000 lx) and 1 sun spectra

	3000 K LED		1 sun
Irradiance [W m^{-2}]	0.53	52.12	1000
Lux [lx]	151.63	14 983.54	109 870
PCE [%]	13.38	15.61	8.46
FF [%]	71.09	63.48	51.41
P_{mpp} [mW]	0.07	8.48	88.11
V_{mpp} [V]	2.1	2.5	2.4
I_{mpp} [mA]	0.03	3.39	36.71
V_{OC} [V]	2.53	3.34	3.63
I_{sc} [mA]	0.04	4	47.22
R_s [Ω]	4627.77	143.9	25.24
R_{sh} [Ω]	1 427 642.44	19 990.5	1303.22
Area [cm^2]	10.42	10.42	10.42

Battery characterization. The sodium battery comprised sodium titanium phosphate (NTP) directly deposited on carbon nanotube cloth as a cathode (NTP@CNT), a metallic sodium anode and 1 M $NaPF_6$ in diglyme (diethylene glycol dimethyl ether, DEGDME) as the electrolyte with two Celgard® separators. The battery was separately characterized prior to the combined tests under potential limited galvanostatic charge–discharge cycles under increasing current rates (Fig. 2).

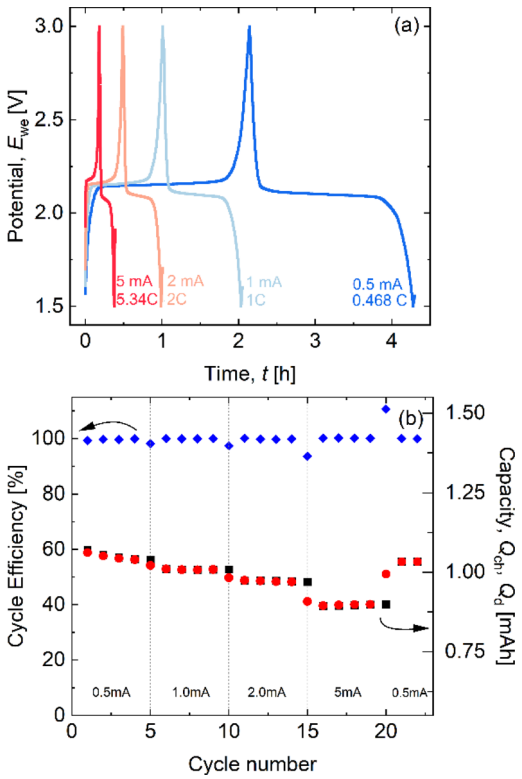

Fig. 2 (a) Charge–discharge curves at different current rates with respect to time. (b) Cycle efficiency (blue diamonds, left axis) and capacity stored (red circles) and discharged (black squares) in mA h (right axis) *vs.* cycle number.

Fig. 2a shows the voltage of the battery over time under different charge and discharge rates. Most of the battery charge capacity is within the plateau region between 2.14 V and 2.19 V, and for the charge rate up to 5C, there is no noticeable increase in battery voltage. Most of the battery discharge capacity is within the plateau region between 2.06 V and 2.12 V. The small difference between charge and discharge voltage plateaus indicates low overpotentials even at elevated charging and discharging rates.

Fig. 2b shows the charge and discharge capacities and the coulombic efficiency of each cycle. The 1.76 cm^2 battery electrode was operated under approximately 0.5–5C galvanostatic charge rates using 1.5 and 3.0 V as cutoff voltages. Coulombic efficiencies recorded for cycles with equal charge and discharge rates range between 99.2% and 99.9%.

Direct charge–discharge test of the PV-battery device

The performance of the OPV module coupled with the battery was investigated in a setup encompassing a switched resistor circuit, ammeter, and voltmeter (see Fig. S3†). Prior to the test, the battery was discharged down to 2.09 V. The battery was charged for 400 s at each light intensity before being discharged based on the charge stored.

Fig. 3a shows the battery charge and discharge voltage profiles over time driven by the PV module under different illuminance levels from 150 lx up to 15 000 lx. From this we can deduce the voltage difference between charge and discharge. The maximum difference between the highest point of the

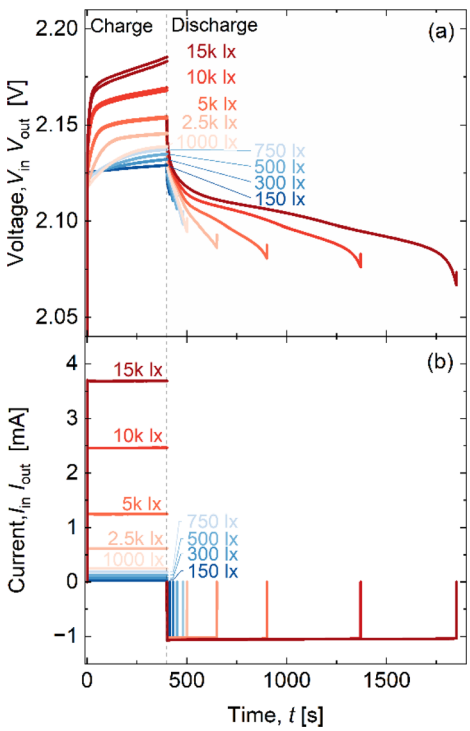

Fig. 3 (a) Voltage–time curves for the direct charging of the NTP half-cell with the PM6:Y6:PCBM 5-cell module under various LED illumination intensities. (b) Current *vs.* time of the same tests.

charge curve and the lowest point of the discharge curve is approximately 0.1 V, which is approximately 5% of the nominal cell voltage of 2.12 V. Despite the absence of current control in either charge or discharge, the device exhibits an almost constant value in both charge and discharge regimes. This indicates that the system is not only very stable over a wide range of charge rates up to 3.3C but also delivers sustained power over an extended time.

In Fig. 3b, the current of the connected setup measured under various LED illumination intensities is plotted against time. In the first 400 s, the OPV module directly charges the battery: the current is positive. After 400 s, the battery is discharged: the currents are negative. The vertical lines in the current graph signify the beginning and the end of the experiments when the current goes to zero. Under LED illumination at 15 000 lx, the maximum C-rate is 3.3C. The C-rate for the discharge across the 2 kΩ resistor was approximately 1C.

PV-battery device performance

Taking short-circuit current density as a proxy for illumination intensity, we present the performance of the LED charging across varying intensities in Fig. 4 using the previously defined metrics (see ESI† for detailed definition and description of reported metrics). We have highlighted the current density associated with illumination intensities between 150 and 500 lx (in green, Fig. 4), which are in general most realistically reflective of a regular office setting.

As displayed in Fig. 4a, the PV efficiency peaks at an illuminance of 5000 lx, reaching 15.7%. Towards higher illumination intensities, the efficiency slightly decreases due to a reduced fill factor (FF). This is related to the sub-module layout that is appropriate for low-light conditions, but shows series resistance limitations at higher currents[27] (see the Experimental section for more details). Towards lower illuminance, the efficiency also gradually decreases to 13.3% at 150 lx due to the inevitable voltage losses. However, the device exhibits an extremely high shunt resistance, which enables the FF to remain very high even at very low light intensities of 150 lx. The difference between the PV efficiency and the charging efficiency ($\eta_{PV\text{-}batt}$) largely follows the difference between the maximum power point voltage and the charging voltage, which are reflective of variations in coupling factor. Adding the coupling losses with the voltage drop on battery discharge, we achieve overall efficiency values from 13.1% (150 lx) peaking at 14.4% (5000 lx) and ending at 14.28% (15 000 lx), which is an extraordinarily low variance for this large dynamic range.

At low irradiances, the PV–charging efficiency ($\eta_{PV\text{-}batt}$, Fig. 4a) and the overall efficiency trace the module efficiency closely below 750 lx. They start to diverge at higher intensities mainly due to the divergence of the operating/charging voltage (V_c) with the maximum power point voltage (V_{mpp}) (Fig. 4b). The operating voltage is determined by the charging voltage of the battery, which in this case is almost constant (2.13–2.17 V), while V_{mpp} is dependent on illumination intensity and rises with increased intensity. Despite this, the device at hand reaches coupling factors higher than 90% at every tested intensity

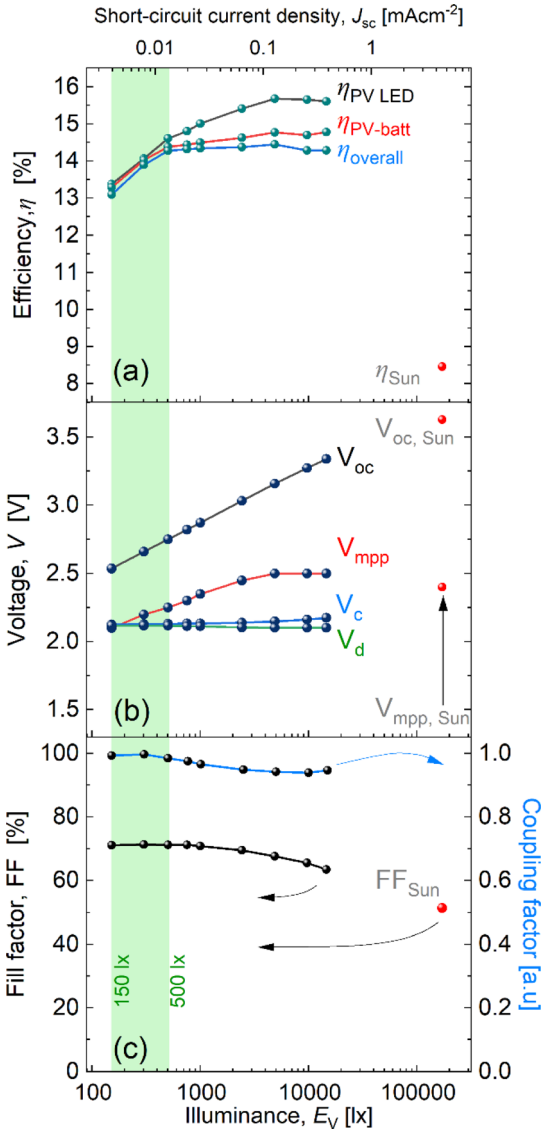

Fig. 4 (a) Efficiency in green dots, (b) voltage in blue dots, and (c) fill factor and coupling factor in black dots *vs.* illuminance values in lux for the LED results of the module. Corresponding short-circuit current density is shown along the top axis. AM1.5 performance of the module is shown in red dots as a comparison and only corresponds with the top axis.

(Fig. 4c). The coupling factor peaks at 0.997 at 300 lx, and dips slightly at 150 lx (to 0.993) due to the battery charging voltage (2.13 V) being slightly higher than the V_{mpp} (2.10 V). As can be seen in Fig. 4b, the charging voltage is lower than the V_{mpp} for all other illumination intensities above 150 lx, and the device follows the design rules we propose in the following section. This exceptionally high degree of power coupling over the whole range of target operating conditions is in line with our previous findings,[1,2,60,61] indicating that no maximum power tracking is required in optimized PV-battery devices. This is most relevant for the small scale indoor light harvesters where power overhead from additional power electronics can potentially lead to significant losses.[1]

For efficient operation we propose and show that the expected charging voltage of the battery at the illumination intensity chosen should be designed/selected to approach as much as possible but not exceed the V_{mpp} of the solar module. This would mean, however, essentially capping the working efficiency of the solar module due to the voltage limitation afforded by the battery. In return, this offers a much wider range of stable efficient operating conditions by operating in the linear rising portion of the solar cell power curve.[60]

Design considerations for optimal direct PV-battery coupling

We analyse and compare the characteristics of both the battery and PV prior to connection and use these to inform our design choices. For the basic design of a direct-coupled PV-battery indoor harvester without control electronics, voltage matching, and relative PV-battery power scaling are related design aspects which directly impact safety and performance. The voltage matching, power coupling and the PV-battery power matching are visualised in two plots shown in Fig. 5. Fig. 5a displays the voltage matching and power coupling aspects, while Fig. 5b illustrates PV-battery power matching. In the left-hand part of Fig. 5a V_{mpp} and open circuit voltage (V_{OC}) of the PV module are plotted against illuminance E_V (bottom x-axis). The teal shaded regions represent operating voltages where PV module output is more than 90% of the maximum (coupling factor > 0.9). In the right-hand part of Fig. 5b (inset), with a shared voltage y-axis, is the battery charging voltage as a function of battery state of charge (top x-axis) for 0.5C and 5C charging rates.

Voltage matching

First, we must ensure that the PV module can charge the battery. The maximum charging voltage is only as high as the V_{OC} of the PV module. From Fig. 5a, the PV module can charge the battery as the V_{OC} is above the charging voltage plateau of the battery (in grey, which is also the expected operating voltage). The expected operating voltage closely matches the results in Fig. 4b. Furthermore, the V_{OC} should not be excessively high compared to the operating voltage of the coupled PV-battery device to expose the battery to voltages leading to instability or degradation (Fig. 5a, inset).

Power coupling (maximizing coupling factor)

To obtain high efficiencies, it must first be acknowledged that the operating voltage of the coupled PV-battery device is determined by the battery, while the charging current is dependent on the PV current at the operating voltage under illumination. Thus, the coupling efficiency, or coupling factor, of the system is then maximal when battery charging voltage equals V_{mpp} of the PV module (eqn (S1)†).[33,62] As opposed to typical outdoor PV systems, in autonomous indoor devices, losses at low irradiance are more important than those at high irradiance. Most of the excess energy potentially available at higher E_V will not be utilised, as the energy consumed by the load must be as low as the worst-case supply. Therefore, a good match between V_{mpp} of the

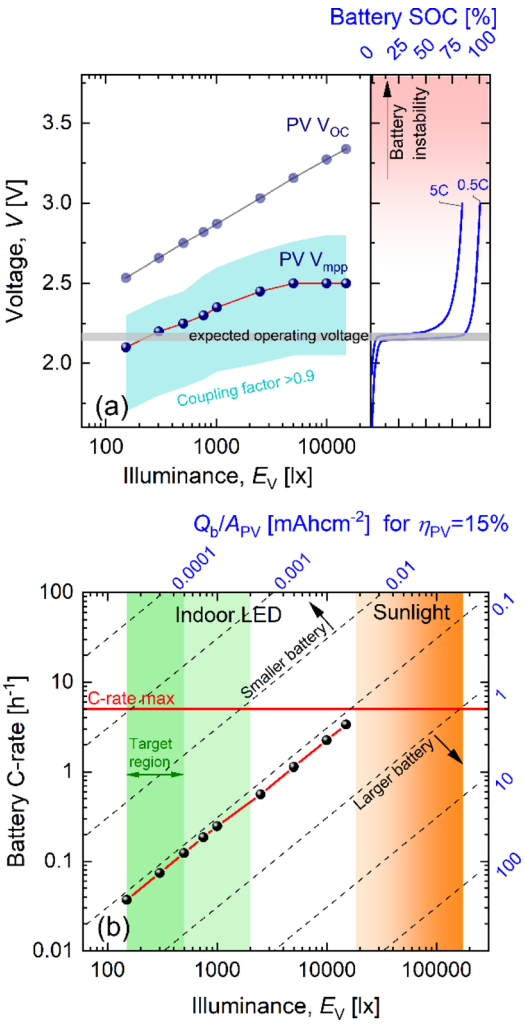

Fig. 5 (a) Voltage: open circuit voltage V_{OC} and maximum power point voltage V_{mpp} of the PV module as a function of illuminance as per Fig. 4b. The blue lines on the right-hand side inset represent battery voltage as a function of state of charge (SOC) for 0.5 and 5C-rate sharing the same voltage axis. The teal region represents operating voltages with coupling factors above 0.9. The grey region is the expected operating voltage of the combined system. (b) Power coupling: the current supplied by the PV module in terms of battery C-rate (black dots, red line) plotted against LED illuminance. Dashed diagonal lines represent charging rate dependence on illuminance (E_V) for a PV-battery device with a PV efficiency of 15%. Orange and green shaded regions indicate typical illuminance regions of indoor LED and sunlight, respectively.

PV module and the charging plateau voltage of the battery is most critical for the lowest illuminance where power is scarce.

In practice, maximizing coupling factor is achieved by designing the solar module V_{mpp} to match the charging voltage of the battery. A narrow range of operating voltages is achieved by having a fast-charging battery material with low overpotentials and a well-defined charging plateau. Low overpotentials result in a steep battery IV curve, while a well-defined charging plateau will ensure a minimal voltage increase across the state of charge of the battery, keeping within the high coupling factor region in Fig. 5a. Combining these principles

with partial usage of the maximum battery capacity by working in the plateau region of the battery results in high efficiencies. In principle, it is possible to tune the battery electrode conductivity to have the V_c trace the V_{mpp} closely, thereby increasing the coupling factor. However, increasing battery charging voltages at higher illumination intensities (currents) will not improve the overall performance as the battery round trip efficiency will simultaneously decrease.

Charging beyond the plateau, as the battery reaches the maximal state of charge and its voltage increases, the operating voltage of the PV module shifts towards V_{OC}, leading to the charging power (and coupling factor) decreasing towards zero, making the direct charging of the battery self-limited.

PV-battery power matching

With voltages for the battery and PV module determined, the next step to ensure high efficiency is to match the power input of the battery with the power output of the PV module. The maximum charging rate that the battery can sustain must be higher than what the PV module can supply and is accomplished by adjusting the capacity of the battery relative to the active area of the PV module. The C-rate and amount of stored energy are two aspects that must be considered to scale the capacity of the battery.

The scaling of battery capacity (Q_b) in relation to PV area (A_{PV}) can be quantified using the ratio Q_b/A_{PV}, which represents a 'PV-specific capacity' expressed in mA h cm^{-2}. We can then express the C-rate of the device at every illuminance by dividing the current density of the PV module by this ratio, assuming a fixed PV efficiency for simplicity. Fig. 5b visualises the C-rate aspect, showing the dependence of battery C-rate, C_b,

$$C_b(E_V) = [A_{PV} \times J_{PV}(E_V)]/(Q_b) \quad (1)$$

on illuminance, where $J_{PV}(E_V)$ is the dependence of PV current density on illuminance.

To provide orientation, we calculated reference dependencies for different values of the Q_b/A_{PV} ratios. The diagonal dashed lines indicate the dependencies of the C-rate on illuminance for decimal multiples of Q_b/A_{PV}, calculated for a constant PV efficiency of 15%, as indicated outside the graph in blue. In relation to our device, the Q_b/A_{PV} ratio is capable of operating from 150 lx to 15 000 lx.

Taking the lowest target illuminance of 150 lx, the PV module produces ~0.0034 mA cm^{-2}. Assuming an illumination period of 10 hours, this translates to a minimum specific capacity of 0.034 mA h cm^{-2} of PV area. The experimental data for our PV-battery device with $Q_b/A_{PV} = 0.11$ mA h cm^{-2} is well above this minimum. The data also aligns well with the guideline for $Q_b/A_{PV} = 0.1$ mA h cm^{-2} in Fig. 5b, even though the PV efficiency is not constant in the experiment. This is because the wide dynamic range of the plot makes deviations in PV efficiency insignificant.

The device presented in this work has been designed in accordance with the aforementioned considerations with an emphasis on performance, thus achieving high overall efficiency. Further development of the PV-battery harvester includes more detailed tailoring of both PV and battery elements for common operation under indoor conditions. In general, there are different optimisation criteria for PV and batteries when used in indoor applications. For OPV devices, thicker absorber layers can increase indoor efficiency due to increased shunt resistance.[63] Also, wider sub-cells of modules can be designed without negatively affecting the performance, since low-light conditions tolerate higher electrode resistances. In contrast, under one sun conditions, both approaches are detrimental due to increased series resistances that will decrease device efficiency, whereas high shunt resistance values become less important in this case. On the battery side, stability against overvoltage, high charge rates and high loading densities are of interest.

Experimental

Solar module preparation and layout

The organic solar module (Fig. 6) with 50 mm × 50 mm aperture area was processed on a 75 mm × 75 mm glass/ITO substrate. Zinc oxide nanoparticles (ZnO) and PM6:Y6:PCBM were used as the electron transport layer and photoactive layer, respectively, and processed from solution by blade coating. Molybdenum oxide (MoO_x) and silver (Ag) were used as the hole transport layer and electrode, respectively, and deposited by thermal evaporation. The module was structured with a classical P1, P2, and P3 pattern using a nanosecond laser (see the sketch in Fig. 6). A detailed description of the module manufacturing processes and materials has been previously published.[59]

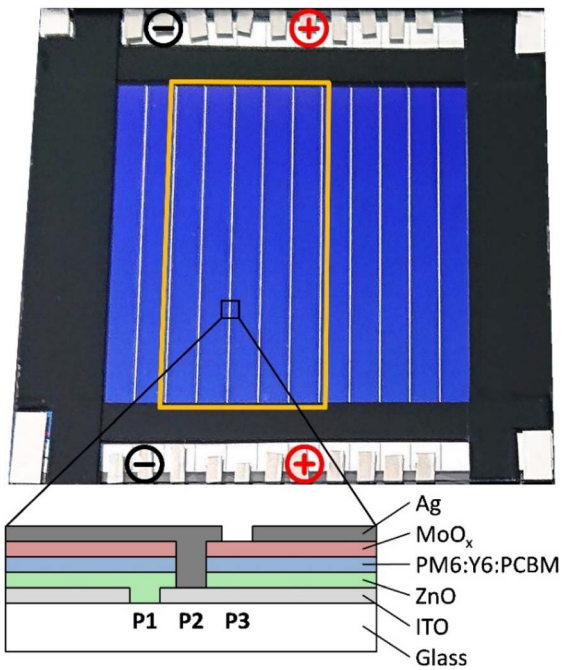

Fig. 6 OPV module with 12 cells. Placing the contacts as shown creates and measures a 5-cell sub-module (indicated by the orange frame).

The final OPV module is shown in Fig. 6 together with a scheme of its cross-section. The full module comprises 12 sub-cells connected in series, of which each cell can be contacted individually at the top and the bottom. Like this, a variety of sub-modules with any desired number of cells ranging from 1 to 12 can be created and measured by varying the contacting positions. It is of note, however, that for any cell number other than all 12, the current cannot be extracted by the two big vertical busbars that are applied on the very left and right side of the module but must be extracted to the top and bottom through a 4 mm narrow and 100 nm thick silver electrode of one of the sub-cells. This leads to significant series resistance losses for high current densities (*e.g.* 1 sun), as can be seen by a decrease in FF with increasing light intensity (see Fig. 4c). In the illumination regime that is most interesting for this present work (<1000 lx), no series resistance limitations are observed (FF > 70%).

This versatile module layout enables us to choose the number of sub-cells that provides a voltage output that best possibly fits the charging voltage of the sodium ion battery. In this work, we use a 10.42 cm^2 5-cell sub-module (as indicated by the orange frame) by placing the contacts as indicated by the black and red minus and plus symbols, respectively.

Battery electrode preparation

The battery electrodes were prepared as previously described[1] with no modification to the technique and are presented here again for the convenience of the reader. All chemical reagents (of analytical grade) were purchased from Sigma-Aldrich and used as received if not otherwise specified.

Sodium-ion batteries were made from a sodium metal anode, sodium titanium phosphate cathode ($NaTi_2(PO_4)_3$, NTP), and 1 M $NaPF_6$ in bis(2-methoxyethyl) ether (diethylene glycol dimethyl ether, DEGDME) electrolyte. Sodium titanium phosphate was drop coated onto carbon nanotube (CNT) cloth.[64,65]

A4-sized CNT non-woven mats with a thickness of 115 mm were obtained from Tortech Nano-Fibers (Ma'alot-Tarshiha, Israel). These were cut and cleaned with concentrated hydrochloric acid and a mixture of ethanol/water (1 : 1, v/v).

A precursor solution of NaTi–P–O was prepared by the dropwise addition of titanium(IV) isopropoxide (~0.05 mol) to ammonium hydroxide (30 mL) under vigorous stirring until a white gelatinous precipitate formed. The suspension was washed with 500 mL deionized water under vacuum filtration to remove excess base and then dissolved in 1 M oxalic acid (200 mL) at 60 °C and stirred until a colourless solution of $H_2[TiO(C_2O_4)_2]$ was formed. 5% stoichiometric excess sodium acetate and a stoichiometric amount of ammonium dihydrogen phosphate were first separately mixed and dissolved in water. This mixture was added slowly to the transparent solution in oxalic acid to yield a colourless and slightly cloudy suspension.

The precursor solution (1 mL) was drop coated onto the 100 cm^2 squares of CNT cloth using a micropipette and dried at 100 °C for 2 h in a vacuum drying oven, which was repeated twice. The coated CNT cloth was then carbonized at 800 °C for 8 h in a tube furnace under Ar flow (~20 sccm). NTP@CNT electrodes were then pressed at 30 MPa in a polyethylene zip-lock bag. The prepared electrode thickness was around 130 mm, and the mass loading of both electrodes was a minimum of 7.5 mg cm^{-2}. The electrode sheets were then dried *in vacuo* in a Buchi oven for at least 2 h at 120 °C.

Battery assembly

The electrochemical properties of the prepared electrodes were assessed in a steel CR2032 coin cell. The assembly of all the test cells was conducted in an argon glovebox, where the concentrations of water and oxygen were kept at less than 0.1 ppm. The 15 mm diameter electrodes (1.767 cm^2) were cut directly from the prepared sheets, weighed, and then used without further modification. Metallic sodium foil was used as the counter electrode and pressed onto 15 mm stainless steel discs. Batteries were made with 1 M $NaPF_6$ in 2-methoxyethyl ether (diethylene glycol dimethyl ether, DEGDME, or diglyme) electrolyte and two 16 mm diameter Celgard® separators. The electrolyte was dried with molecular sieves at least 1 day after preparation and kept with molecular sieves in a sealed bottle within the glove box thereafter to eliminate any trace water content, which was essential to ensure reproducible results.

Three-terminal PV-battery test setup

The solar module is linked to the battery and two Keithley source measurement units acting as an ammeter and voltmeter, *via* a separate switch box with a 2 kΩ resistor. This setup allows for the disconnection of the solar module from the battery for standalone solar cell testing or standalone battery discharge of the battery across the resistor. Data is logged in real time, and all switches and source measurement units are controlled by custom software built in-house. The solar module employed five sub-cells to achieve the required voltage needed to charge the battery.

One sun IV tests under AM1.5G illumination (AM1.5G spectrum, 1000 mW cm^{-2}) were done using a class-A sun simulator from Wacom calibrated monthly. LED charging tests were performed under four XLamp® CMA1840 LED, specifically CMA1840-0000-000N0U0A30G LED-ARRAY, COB, WW, 3000 K, 4481LM 38.2 W (Cree LED. 4001 E. Hwy. 54, Suite 2000, Durham, NC 27709 USA. **https://www.cree-led.com**) placed in a 2 × 2 array 50 cm from the module in a measurement chamber. The LED array was connected to an EA-PS 5080-20 A power supply from Elektro-Automatik which was electronically controlled to vary the intensity of the array and calibrated prior to the test. LED intensity and spectrum were measured using a spectral analyser before each set of measurements (Fig. S4–S7†). The LED array was measured from low to high intensities and allowed to stabilize for 180 s between each intensity change to allow for thermal stabilization. The battery cell was discharged for 1800 s prior to all tests to ensure that the cell was within the working plateau throughout the tests and maximum discharge time was within this time. Charge time was fixed at 400 s. The battery was discharged across the 2 kΩ resistor during discharge for variable times depending on the amount of charge accumulated during charging. All IV scans were done

with no dwell time and a 20 ms integration time per step at 0.02 V per step (1 V s^{-1} sweep rate).

Conclusions

We demonstrate a sodium ion battery directly charged by an organic photovoltaic module, achieving overall system efficiencies exceeding 10% under indoor illumination for the first time. Under 3000 K warm white LED illumination between 150 and 15 000 lx we achieve a PV efficiency between 13.37% and 15.67% using a 5-cell PM6:Y6:PCBM organic solar module. Using this to charge a sodium ion battery, almost 100% coupling efficiency over the full range of target conditions of 150–500 lx with only a mild increase in coupling loss under higher irradiance is realized, all with direct coupling without any power conditioning electronics or maximum power point tracker. The resulting overall efficiencies of the coupled PV-battery device ranged from 13.1% to 14.4%. These high efficiencies are achieved due to the persistent FF of the OPV module under low light and *via* proper system design. The maximum power point voltage range is aligned with the battery charging voltage range in low light conditions of interest. Overall, the combination of OPV with Na-ion batteries seems to be a very suitable candidate for a variety of IoT applications and deeper integration of both devices must be explored.

We then illustrate in detail the design considerations of voltage matching, power coupling and, PV-battery power matching that we used to achieve these high results. Our work shows that the choice of battery material is not only important to have a matching voltage, but also essential to achieve a high efficiency. A high rate-capability material is necessary for a wide range of high efficiency and low overpotential losses at higher rates of charge/illumination. Battery materials with flat voltage profiles akin to well defined plateaus are also preferable for stable operation of the solar cell and predictable charging currents and operating points. These design considerations are not limited to organic photovoltaics or sodium batteries and can be applied to any type of PV and battery system.

Comparing our results to previous attempts (Table S1†) at using an organic PV module coupled to a battery, we report the highest efficiency regardless of irradiance. This is despite utilizing a very low powered LED irradiance just above 5 mW cm^{-2}. This highlights either that there are serious losses related to integration in the reported devices, or that there is a fundamental lacking in the design process and/or compatibility between PV and battery components. We address the latter point with consideration to optimal PV-battery design.

A further increase in efficiencies can be achieved by optimizing the PV module design and absorber layer, such as using higher band gap absorber materials. This has a two-fold benefit. Firstly, higher band gap materials will have absorption spectra that match the LED spectrum more closely. Secondly, the higher voltage will require lesser sub-cells per module and thus result in a higher current output at the same module size or a smaller module at constant current.

We hope our results will serve as a framework and benchmark for future light-based power harvesters to power IOT devices or other always-on low powered devices.

Data availability

Data for this article, including spectral data of light sources, LED calibration data, PV characterization data under LED and AM1.5, battery characterization data and charge–discharge data, are available at **https://www.Zenodo.org** at **https://doi.org/10.5281/zenodo.12657217**.

Author contributions

Li-Chung Kin: writing-original draft, conceptualization, data curation, formal analysis, writing-review & editing, investigation, validation, visualization, methodology. Bakary Kone: investigation, visualization. Dr Andreas Distler: visualization, writing-review & editing. Dr Oleksandr Astakhov: writing-review, visualization, & editing, conceptualization, formal analysis, methodology. Dr Hans Kungl: supervision, project administration, writing-review, funding acquisition. Dr Andre Karl: project administration, writing-review & editing. Dr Tsvetelina Merdzhanova: conceptualization, writing-review & editing, supervision, project administration, funding acquisition. Prof. Dr Rüdiger-A. Eichel: funding acquisition, resources. Prof. Dr Christoph J. Brabec: writing-review & editing, funding acquisition, resources. Prof. Dr Uwe Rau: funding acquisition, resources.

Conflicts of interest

There are no conflicts to declare.

Acknowledgements

The authors would like to acknowledge the contribution of Christoph Zahren for technical, software support, guidance, and calibration of the LED source. And Sebastian B. C. Lehmann for the work on the TOC picture. A. D. and C. J. B. acknowledge funding from the European Union's Horizon 2020 Research and Innovation Program (H2020 Societal Challenges) under the grant numbers 952911 (BOOSTER) and 101007084 (CITYSOLAR). The authors acknowledge the DFG funded graduate school with Nagoya (ITRG 2495) as well as the DFG funded research group (Forschergruppe) POPULAR (BR 4031/25-1) for funding and support.

Notes and references

1 L.-C. Kin, Z. Liu, O. Astakhov, S. Shcherbachenko, H. Kungl, T. Kirchartz, R.-A. Eichel, U. Rau and T. Merdzhanova, *Cell Rep. Phys. Sci.*, 2022, **3**, 101123.
2 S. Shcherbachenko, O. Astakhov, U. Chime, L.-C. Kin, K. Ding, B. Pieters, U. Rau, E. Figgemeier and T. Merdzhanova, *Sol. RRL*, 2023, **7**, 2200857.

3 K. S. Srivishnu, M. N. Rajesh, S. Prasanthkumar and L. Giribabu, *Sol. Energy*, 2023, **264**, 112057.
4 H. K. H. Lee, Z. Li, J. R. Durrant and W. C. Tsoi, *Appl. Phys. Lett.*, 2016, **108**, 253301.
5 G. Kumar and F.-C. Chen, *J. Phys. D: Appl. Phys.*, 2023, **56**, 353001.
6 X. Hou, Y. Wang, H. K. H. Lee, R. Datt, N. Uslar Miano, D. Yan, M. Li, F. Zhu, B. Hou, W. C. Tsoi and Z. Li, *J. Mater. Chem. A*, 2020, **8**, 21503–21525.
7 S. Biswas and H. Kim, *Polymers*, 2020, **12**, 1338.
8 G. Lucarelli, F. Di Giacomo, V. Zardetto, M. Creatore and T. M. Brown, *Nano Res.*, 2017, **10**, 2130–2145.
9 M. Li, F. Igbari, Z.-K. Wang and L.-S. Liao, *Adv. Energy Mater.*, 2020, **10**, 2000641.
10 P. A. Mini, S. V. Nair and K. R. V. Subramanian, *Prog. Photovoltaics*, 2013, **21**(5), 1153–1157.
11 Y. Cui, H. Yao, J. Zhang, T. Zhang, Y. Wang, L. Hong, K. Xian, B. Xu, S. Zhang, J. Peng, Z. Wei, F. Gao and J. Hou, *Nat. Commun.*, 2019, **10**, 2515.
12 C. Li, X. Gu, Z. Chen, X. Han, N. Yu, Y. Wei, J. Gao, H. Chen, M. Zhang, A. Wang, J. Zhang, Z. Wei, Q. Peng, Z. Tang, X. Hao, X. Zhang and H. Huang, *J. Am. Chem. Soc.*, 2022, **144**, 14731–14739.
13 L. Zhu, M. Zhang, J. Xu, C. Li, J. Yan, G. Zhou, W. Zhong, T. Hao, J. Song, X. Xue, Z. Zhou, R. Zeng, H. Zhu, C.-C. Chen, R. C. I. MacKenzie, Y. Zou, J. Nelson, Y. Zhang, Y. Sun and F. Liu, *Nat. Mater.*, 2022, **21**, 656–663.
14 J. Fu, P. W. K. Fong, H. Liu, C.-S. Huang, X. Lu, S. Lu, M. Abdelsamie, T. Kodalle, C. M. Sutter-Fella, Y. Yang and G. Li, *Nat. Commun.*, 2023, **14**, 1760.
15 X. Dong, Y. Jiang, L. Sun, F. Qin, X. Zhou, X. Lu, W. Wang and Y. Zhou, *Adv. Funct. Mater.*, 2022, **32**, 2110209.
16 R. Sun, T. Wang, X. Yang, Y. Wu, Y. Wang, Q. Wu, M. Zhang, C. J. Brabec, Y. Li and J. Min, *Nat. Energy*, 2022, **7**, 1087–1099.
17 S. Dong, T. Jia, K. Zhang, J. Jing and F. Huang, *Joule*, 2020, **4**, 2004–2016.
18 H. Chen, R. Zhang, X. Chen, G. Zeng, L. Kobera, S. Abbrent, B. Zhang, W. Chen, G. Xu, J. Oh, S.-H. Kang, S. Chen, C. Yang, J. Brus, J. Hou, F. Gao, Y. Li and Y. Li, *Nat. Energy*, 2021, **6**, 1045–1053.
19 A. Distler, *The Most Efficient Organic Solar Module in the World comes from FAU and HI ERN*, **https://www.fau.eu/2023/12/19/news/research/world-record-in-solar-energy/**, accessed 29 January 2024, 2024.
20 R. Basu, F. Gumpert, J. Lohbreier, P.-O. Morin, V. Vohra, Y. Liu, Y. Zhou, C. J. Brabec, H.-J. Egelhaaf and A. Distler, *Joule*, 2024, **8**(4), 970–978.
21 L.-c. Kin, Z. Liu, O. Astakhov, S. N. Agbo, H. Tempel, S. Yu, H. Kungl, R.-A. Eichel, U. Rau, T. Kirchartz and T. Merdzhanova, *ACS Appl. Energy Mater.*, 2019, **3**, 431–439.
22 S. Castro-Hermosa, G. Lucarelli, M. Top, M. Fahland, J. Fahlteich and T. M. Brown, *Cell Rep. Phys. Sci.*, 2020, **1**, 100045.
23 S. Biswas, Y. Lee, H. Choi, H. W. Lee and H. Kim, *RSC Adv.*, 2023, **13**, 32000–32022.
24 H. S. Ryu, S. Y. Park, T. H. Lee, J. Y. Kim and H. Y. Woo, *Nanoscale*, 2020, **12**, 5792–5804.
25 M. A. Alkhalayfeh, A. Abdul Aziz, M. Z. Pakhuruddin, K. M. M. Katubi and N. Ahmadi, *Phys. Status Solidi A*, 2022, **219**, 2100639.
26 M. Jahandar, S. Kim and D. C. Lim, *ChemSusChem*, 2021, **14**, 3449–3474.
27 Y. Cui, L. Hong and J. Hou, *ACS Appl. Mater. Interfaces*, 2020, **12**, 38815–38828.
28 C. L. Cutting, M. Bag and D. Venkataraman, *J. Mater. Chem. C*, 2016, **4**, 10367–10370.
29 R. Arai, S. Furukawa, N. Sato and T. Yasuda, *J. Mater. Chem. A*, 2019, **7**, 20187–20192.
30 S. K. Thomas, A. Pockett, K. Seunarine, M. Spence, D. Raptis, S. Meroni, T. Watson, M. Jones and M. J. Carnie, *IoT*, 2022, **3**, 109–121.
31 Y. Aoki, *Org. Electron.*, 2017, **48**, 194–197.
32 VentureRadar, *Top OPV Companies*, **https://www.ventureradar.com/keyword/OPV**, accessed 19-01, 2024.
33 F. Sandbaumhüter, S. N. Agbo, C.-L. Tsai, O. Astakhov, S. Uhlenbruck, U. Rau and T. Merdzhanova, *J. Power Sources*, 2017, **365**, 303–307.
34 S. N. Agbo, T. Merdzhanova, U. Rau and O. Astakhov, *Sol. Energy Mater. Sol. Cells*, 2017, **159**, 427–434.
35 S. N. Agbo, T. Merdzhanova, S. Yu, H. Tempel, H. Kungl, R.-A. Eichel, U. Rau and O. Astakhov, *J. Power Sources*, 2016, **327**, 340–344.
36 D. Lübke, P. Hartnagel, J. Angona and T. Kirchartz, *Adv. Energy Mater.*, 2021, **11**, 2101474.
37 M. Lee, E. Choi, A. M. Soufiani, J. Lim, M. Kim, D. Chen, M. A. Green, J. Seidel, S. Lim, J. Kim, X. Dai, R. Lee-Chin, B. Zheng, Z. Hameiri, J. Park, X. Hao and J. S. Yun, *Adv. Funct. Mater.*, 2021, **31**, 2008908.
38 J. Yuan, Y. Zhang, L. Zhou, G. Zhang, H.-L. Yip, T.-K. Lau, X. Lu, C. Zhu, H. Peng, P. A. Johnson, M. Leclerc, Y. Cao, J. Ulanski, Y. Li and Y. Zou, *Joule*, 2019, **3**, 1140–1151.
39 G. Jarosz, M. Franz, R. Marczyński and R. Signerski, *Org. Electron.*, 2021, **88**, 105999.
40 J. K. W. Ho, H. Yin and S. K. So, *J. Mater. Chem. A*, 2020, **8**, 1717–1723.
41 A. S. Teran, J. Wong, W. Lim, G. Kim, Y. Lee, D. Blaauw and J. D. Phillips, *IEEE Trans. Electron Devices*, 2015, **62**, 2170–2175.
42 I. Mathews, S. N. Kantareddy, T. Buonassisi and I. M. Peters, *Joule*, 2019, **3**, 1415–1426.
43 K. Rühle and M. Kasemann, Approaching high efficiency wide range silicon solar cells, *2013 IEEE 39th Photovoltaic Specialists Conference (PVSC)*. Tampa, FL, USA, 2013, pp. 2651–2654, DOI: **10.1109/PVSC.2013.6745018**.
44 M. Freunek, M. Freunek and L. M. Reindl, *IEEE Journal of Photovoltaics*, 2013, **3**, 59–64.
45 W. Wang, Y. Cui, T. Zhang, P. Bi, J. Wang, S. Yang, J. Wang, S. Zhang and J. Hou, *Joule*, 2023, **7**, 1067–1079.
46 T. H. Kim, N. W. Park, M. A. Saeed, S. Y. Jeong, H. Y. Woo, J. Park and J. W. Shim, *Nano Energy*, 2023, **112**, 108429.
47 Q. Wu, Y. Yu, X. Xia, Y. Gao, T. Wang, R. Sun, J. Guo, S. Wang, G. Xie, X. Lu, E. Zhou and J. Min, *Joule*, 2022, **6**, 2138–2151.

48 G. R. Newsham and J. A. Veitch, *Lighting Research & Technology*, 2001, **33**, 97–113.
49 W. Li, H.-C. Fu, Y. Zhao, J.-H. He and S. Jin, *Chem*, 2018, **4**, 2644–2657.
50 Y. Hu, Y. Bai, B. Luo, S. Wang, H. Hu, P. Chen, M. Lyu, J. Shapter, A. Rowan and L. Wang, *Adv. Energy Mater.*, 2019, 1900872.
51 J. Xu, Y. Chen and L. Dai, *Nat. Commun.*, 2015, **6**, 8103.
52 H.-D. Um, K.-H. Choi, I. Hwang, S.-H. Kim, K. Seo and S.-Y. Lee, *Energy Environ. Sci.*, 2017, **10**, 931–940.
53 P. Chen, T.-T. Li, Y.-B. Yang, G.-R. Li and X.-P. Gao, *Nat. Commun.*, 2022, **13**, 64.
54 H. Sun, Y. Jiang, S. Xie, Y. Zhang, J. Ren, A. Ali, S.-G. Doo, I. H. Son, X. Huang and H. Peng, *J. Mater. Chem. A*, 2016, **4**, 7601–7605.
55 W. Guo, X. Xue, S. Wang, C. Lin and Z. L. Wang, *Nano Lett.*, 2012, **12**, 2520–2523.
56 R. Delgado Andrés, R. Wessling, J. Büttner, L. Pap, A. Fischer, B. Esser and U. Würfel, *Energy Environ. Sci.*, 2023, **16**, 5255–5264.
57 V. Chakrapani, F. Rusli, M. A. Filler and P. A. Kohl, *J. Power Sources*, 2012, **216**, 84–88.
58 S. F. Hoefler, R. Zettl, D. Knez, G. Haberfehlner, F. Hofer, T. Rath, G. Trimmel, H. M. R. Wilkening and I. Hanzu, *ACS Sustain. Chem. Eng.*, 2020, **8**, 19155–19168.
59 A. Distler, C. Brabec and H. J. Egelhaaf, *Prog. Photovoltaics*, 2021, **29**(1), 24–31.
60 O. Astakhov, T. Merdzhanova, L.-C. Kin and U. Rau, *Sol. Energy*, 2020, **206**, 732–740.
61 U. Chibuko, T. Merdzhanova, D. Weigand, F. Ezema, S. Agbo, U. Rau and O. Astakhov, *Sol. Energy*, 2023, **249**, 233–241.
62 L. C. Kin, Z. F. Liu, O. Astakhov, S. N. Agbo, H. Tempel, S. C. Yu, H. Kungl, R. A. Eichel, U. Rau, T. Kirchartz and T. Merdzhanova, *ACS Appl. Energy Mater.*, 2020, **3**, 431–439.
63 D. Lübke, P. Hartnagel, M. Hülsbeck and T. Kirchartz, *ACS Mater. Au*, 2023, **3**, 215–230.
64 S. Yu, Z. Liu, H. Tempel, H. Kungl and R.-A. Eichel, *J. Mater. Chem. A*, 2018, **6**, 18304–18317.
65 Y. Fang, J. Zhang, L. Xiao, X. Ai, Y. Cao and H. Yang, *Adv. Sci.*, 2017, **4**, 1600392.